

# Modelling Dynamic Ice Sheet Boundaries and Grounding Line Migration using the Level Set Method

M. Alamgir HOSSAIN,<sup>1</sup> Sam PIMENTEL,<sup>2</sup> John M. STOCKIE<sup>1</sup>

<sup>1</sup>*Department of Mathematics, Simon Fraser University, Burnaby, BC, Canada*

<sup>2</sup>*Department of Mathematical Sciences, Trinity Western University, Langley, BC, Canada*

*Correspondence: M. Alamgir Hossain <mahossai@sfu.ca>*

**ABSTRACT.** Computing predictions of future sea-level that include well-defined uncertainty bounds requires models that are capable of robustly simulating the evolution of ice sheets and glaciers. Ice flow behaviour is known to be sensitive to the location and geometry of dynamic ice boundaries such as the grounding line, terminus position and ice surface elevation, so that any such model should track these interfaces with a high degree of accuracy. To address this challenge we implement a numerical approach that uses the level set method (LSM) that accurately models the evolution of the ice-air and ice-water interface as well as capturing topological changes in ice sheet geometry. This approach is evaluated by comparing simulations of grounded and marine terminating ice sheets to various analytical and numerical benchmark solutions. A particular advantage of the LSM is its ability to explicitly track the moving margin and grounding line whilst using a fixed grid finite-difference scheme. Our results demonstrate that the LSM is an accurate and robust approach for tracking the ice surface interface and terminus for advancing and retreating ice sheets, including the transient marine ice sheet interface and grounding line positions.

## 24 1. INTRODUCTION

25 The Greenland and Antarctic ice sheets have been losing mass at an accelerated rate (Bevis and others,  
 26 2019; Rignot and others, 2019) and ice sheet margins have recently undergone dramatic changes (Bunce  
 27 and others, 2018; Konrad and others, 2018). These ice sheets are expected to experience further significant  
 28 changes into the future (e.g. Edwards and others, 2019). These rapid dynamic changes are occurring not  
 29 through the slow internal deformation of ice under the force of gravity but rather because of interactions  
 30 between ice bodies and their boundaries. Whether that be ice-bed, such as hydrologically-accelerated basal  
 31 sliding (e.g. Schoof, 2010); ice-ocean, such as submarine melt induced by subglacial discharge and/or  
 32 fjord temperature (e.g. Jenkins, 2011; Straneo and Heimbach, 2013); or ice-air, through mass-balance  
 33 feedbacks (e.g. Vizcaino and others, 2015). Ice flow dynamics are known to be very sensitive to the interface  
 34 locations; for example, the stability of marine ice sheets depends fundamentally on the grounding line  
 35 position (Schoof, 2007). Consequently careful attention must be paid to these interfaces when modelling  
 36 ice sheet flow. In particular, any choice of numerical algorithm must be guided by the need to accurately  
 37 capture dynamically evolving boundaries, and hence to ensure reliable predictions of ice volume and extent  
 38 and to minimize uncertainty in sea level rise estimates.

39 To address these challenges, we aim to demonstrate that the level set method is an effective approach for  
 40 accurately tracking the evolution of the ice-air and ice-water interfaces, as well as the terminus position for  
 41 ice sheets and the grounding line position of marine ice sheets. The level set approach is versatile and can  
 42 be incorporated into any ice sheet model (shallow ice to full Stokes) regardless of numerical discretization  
 43 of the governing equations (finite difference or finite element, fixed grid or adaptive mesh). In this paper  
 44 we present a level set method implemented in shallow ice models using a finite difference discretisation on  
 45 a fixed rectangular grid.

The evolution of an ice sheet free surface is typically modelled by solving the kinematic boundary  
 condition

$$\frac{\partial \eta}{\partial t} + u \frac{\partial \eta}{\partial x} + v \frac{\partial \eta}{\partial y} - w = \mathcal{M}_j, \quad (1)$$

46 where  $\eta = h(x, y, t)$  for the surface elevation of the ice-air interface or  $\eta = b(x, y, t)$  for the elevation of  
 47 the bottom ice-water interface,  $(u, v, w)$  are the ice velocity components, and  $\mathcal{M}_j(x, y, t)$  denotes the  
 48 (surface  $\mathcal{M}_h$  or bottom  $\mathcal{M}_b$ ) mass balance function. We note that the geometry of an evolving ice-air  
 49 or ice-water interface may experience overriding, breaking, merging, separation, discontinuities, vertical  
 50 fronts, and overhangs, and such events cannot be resolved in the standard setup. Furthermore, because

51 of discretization, elevations are only evaluated at the grid points, and as such, the exact location of the  
52 terminus and grounding line will fall between grid points and is not tracked explicitly. To improve accuracy,  
53 a fine grid resolution is required, which can become prohibitively expensive. This is particularly apparent for  
54 marine ice sheets where fixed-grid methods have been shown to be inadequate in capturing grounding line  
55 migration (Vieli and Payne, 2005; Pattyn and others, 2012; Seroussi and others, 2014). Consequently, ice  
56 sheet modellers have incorporated various approaches to more accurately track the grounding line. These  
57 include grid refinement near the grounding line (e.g. Durand and others, 2009b; Cornford and others,  
58 2013), requiring adaptive remeshing with each displacement of the grounding line. The use of sub-element  
59 parameterizations together with mesh refinement has been shown to be beneficial (Seroussi and others,  
60 2014), although even here the exact grounding line position is not being tracked. Explicit tracking methods  
61 include coordinate stretching to transform the moving boundary onto a fixed domain using a prognostic  
62 equation for grounding line migration (e.g. Hindmarsh, 1996). However, this approach cannot be generalized  
63 to 2-D because of complications in handling the complex evolving geometry of the grounding line. Other  
64 alternatives include the location-based moving mesh approach of Goldberg and others (2009) where the  
65 challenge is to define a suitable monitor function to position nodes, or the velocity-based moving-point  
66 approach proposed by Bonan and others (2016) to track the ice sheet margin, but not yet applied to  
67 addressing the grounding line problem.

68 These difficulties addressed above can be readily handled by the use of the level set method (LSM) which  
69 can capture complex evolving geometries without requiring adaptive mesh refinement, and with the further  
70 advantage of being relatively straightforward to implement. The LSM is an increasingly popular tool within  
71 computational fluid dynamics for tracking the motion of dynamic fluid interfaces and is finding widespread  
72 use in many applications (Sethian, 1999b; Gibou and others, 2018). Level set methods were first applied in  
73 glaciology by Pralong and Funk (2004), who proposed the LSM with the ice-air flow problem as a means  
74 of evaluating the steady-state geometry of a glacier. Further consideration of the applicability of LSM to  
75 ice flow, compared amongst other numerical algorithms for free surface flows, can be found in Caboussat  
76 and others (2011). More recently, Bondzio and others (2016) used a LSM to simulate the migration of the  
77 calving front in a 2-D plan-view modelling study (see also Bondzio and others (2018)). They demonstrate  
78 the benefit of the LSM for simulating calving front dynamics in Jakobshavn Isbræ, west Greenland.

79 In this study, we build on the pioneering exploratory study of Pralong and Funk (2004) by providing  
80 an extensive series of simulations testing the accuracy of the LSM for tracking evolving land- and marine-

81 terminating ice sheet boundaries. We use flow-line and radial ice flow models together with the LSM to  
 82 simultaneously model ice elevations, continental margins, grounding lines and shelf fronts. We highlight  
 83 implementation details not previously addressed such as the use of the signed distance function, calculation  
 84 of extended velocities, and the fast marching method for reinitialization. In Pralong and Funk (2004)  
 85 and Bondzio and others (2016) the LSM is implemented using the finite element method on unstructured  
 86 meshes. Instead, our implementation uses the finite difference method on a regular fixed grid, which further  
 87 highlights the strength and versatility of the LSM by demonstrating that moving ice boundaries can be  
 88 tracked accurately without requiring local mesh refinement.

## 89 2. LEVEL SET METHOD

90 In level set methods, the interface is represented implicitly using a level set function  $\varphi(\mathbf{x}, t)$  which is a  
 91 differentiable function on a space-time domain  $\Omega \times \mathbb{R}_+$ , where  $\mathbf{x} \in \Omega$  is the spatial domain in 2-D or 3-D.  
 92 The surface itself is represented as the zero isosurface or level set  $\varphi(\mathbf{x}, t) = 0$ , which propagates at a speed  
 93 directed normal to the surface  $\partial\Omega$ .

When tracking the ice–air or ice–water interface for an ice sheet or glacier, we can define a level set  
 function  $\varphi$  with the following properties:

$$\begin{aligned} \varphi(\mathbf{x}, t) < 0 & \quad \text{for } \mathbf{x} \in \Omega_i, \\ \varphi(\mathbf{x}, t) > 0 & \quad \text{for } \mathbf{x} \in \Omega_c, \\ \varphi(\mathbf{x}, t) = 0 & \quad \text{for } \mathbf{x} \in \partial\Omega, \end{aligned} \tag{2}$$

where  $\Omega_i$  represents the region inside the ice body,  $\Omega_c$  is the region outside the ice body (consisting of  
 either air or water), and  $\partial\Omega$  is the ice-air or ice-water interface (see Fig. 1). Any level set function fitting  
 this description (Eqn 2) can be used as an initial condition for the level set evolution equation to track  
 an interface (see Section 2.1). However, we will use a special choice corresponding to the signed distance  
 function (cf. Pralong and Funk, 2004) that is numerically advantageous (Vogl, 2016) and improves mass  
 conservation, compared to other choices (Gibou and others, 2018):

$$\varphi(\mathbf{x}, t) = \begin{cases} -d(\mathbf{x}, \partial\Omega), & \text{if } \mathbf{x} \in \Omega_i, \\ d(\mathbf{x}, \partial\Omega), & \text{if } \mathbf{x} \in \Omega_c. \end{cases} \tag{3}$$

94 The value of the level set function corresponds to the Euclidean distance  $d(\mathbf{x}, \partial\Omega)$  between any given spatial  
 95 location  $\mathbf{x}$  and the corresponding closest point on the interface  $\partial\Omega$ , with the sign chosen as negative for  
 96 inside the ice and positive for outside.

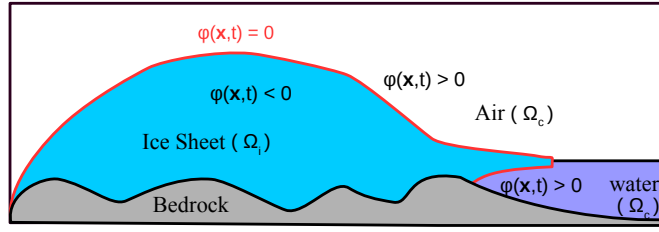


**Fig. 1.** Basic geometry and definition of the level set function  $\varphi(\mathbf{x}, t)$  for a generic ice sheet.

## 97 2.1. Level set evolution

The value of the level set function at any point on an interface with location  $\mathbf{x}(t) \in \Omega$  must satisfy

$$\varphi(\mathbf{x}(t), t) = 0.$$

Differentiating this equation in time and applying the chain rule, we obtain

$$\frac{\partial \varphi}{\partial t} + \nabla \varphi(\mathbf{x}(t), t) \cdot \mathbf{x}'(t) = 0.$$

Supposing that  $F$  is the speed in the outward normal direction, then

$$\mathbf{x}'(t) \cdot \mathbf{n} = F \quad \text{where} \quad \mathbf{n} = \nabla \varphi / \|\nabla \varphi\|.$$

Therefore, the evolution equation for the level set function  $\varphi$  can be written as

$$\frac{\partial \varphi}{\partial t} + F \|\nabla \varphi\| = 0. \quad (4)$$

The normal speed  $F$  should depend on the ice velocity field as well as any accumulation and ablation (Pralong and Funk, 2004). To this end, let  $\mathbf{M}(\mathbf{x}, t)$  denote the mass balance function and  $\mathbf{u}(\mathbf{x}, t)$  the ice velocity field, so that the speed function can be written as

$$F = (\mathbf{u}(\mathbf{x}, t) + \mathbf{M}(\mathbf{x}, t)\hat{z}) \cdot \frac{\nabla \varphi}{\|\nabla \varphi\|}, \quad (5)$$

98 where  $\hat{z}$  is the unit vector in the vertical direction and we have assumed vertical accumulation and  
 99 ablation (Pralong and Funk, 2004).  $\mathbf{M}(\mathbf{x}, t)$  is determined by the surface and basal mass balance functions,  
 100  $\mathcal{M}_h$  and  $\mathcal{M}_b$ , respectively.  $\mathbf{M}(\mathbf{x}, t)$  and  $\mathbf{u}(\mathbf{x}, t)$  can be derived from the specific ice sheet model or fit to  
 101 observational data. The level set equation is solved throughout the computational domain which requires  
 102 speed function values,  $F$ , at all grid points both inside and outside the ice. This necessitates the computing  
 103 of so-called extended speed, the full details of which are provided in Appendix A.1. The numerical

104 implementation of the level set equation is described in Appendix A.2 and we include an explanation  
 105 of a re-initialization procedure that uses the fast marching method (FMM) in Appendix A.3.

## 106 2.2. Coupling between Ice Sheet Model and LSM

107 For the computational experiments performed in this study the LSM described above requires a 2-D ice  
 108 velocity field  $\mathbf{u} = (u, w)$  that comes from an ice flow model, which we obtain using either the shallow ice  
 109 approximation (SIA) or the shallow shelf approximation (SSA), see Appendix B.1 and B.2, respectively.  
 110 The ice velocities  $u$  and  $w$ , the speed function  $F$ , and the level set function  $\varphi$ , are defined on a 2-D grid,  
 111 with the ice thickness  $H$  and the height of the upper surface  $h$  defined on a 1-D grid. The overall solution  
 112 procedure and details regarding the coupling between ice sheet model and the LSM are as follows:

- 113 1. Computing the velocities,  $u^k$  and  $w^k$ : At any time  $t^k$ , the ice thickness  $H^k$  and the height of the upper  
 114 surface  $h^k$  are known.  $H^k$ ,  $h^k$  and the horizontal derivatives of  $h^k$  (determined using the central difference  
 115 approximation) are used to calculate the horizontal and vertical velocities at  $t^k$ ,  $u^k$  and  $w^k$ , respectively.  
 116 In the radially symmetric SIA experiments,  $u^k$  is computed using Eqn (B8) and  $w^k$  using Eqn (B9).  
 117 Whereas for the marine ice sheet and ice shelf experiments, we apply the Picard iteration of the SSA,  
 118 Eqn (B16), to compute  $u^k$ . The derivatives of  $u^k$  and the bedrock are then determined using the central  
 119 difference approximation and  $w^k$  is computed using Eqn (B14), for ice stream, and Eqn (B15), for ice  
 120 shelf.
- 121 2. Computing the speed,  $F^k$ : The velocities,  $u^k$  and  $w^k$ , together with the given surface mass balance  
 122 function, are used to determine  $F^k$  for grid points interior the ice sheet using Eqn (5). For grid points  
 123 exterior to the ice sheet  $F^k$  is determined using the procedure described in Appendix A.1.
- 124 3. Computing  $\varphi^{k+1}$ : The discretized level set evolution Eqn (A5) and the numerical procedure described  
 125 in Appendix A.2 is used to determine the level set at time  $t^{k+1}$ ,  $\varphi^{k+1}$ .
- 126 4. Extract  $H^{k+1}$ : The zero level set is determined with subgrid scale precision from the zero contour line of  
 127  $\varphi^{k+1}$ . The zero level set identifies the ice surface and is used to determine  $H^{k+1}$  and  $h^{k+1}$ . The terminus  
 128 or grounding line position is identified as the location where the zero level set intersects the bottom  
 129 domain boundary. Although we note that our ice velocity solver does not use any subgrid method; for  
 130 example, the exact grounding line position is not used in the SSA computation.

131 5. Re-initialization: The FMM algorithm (Appendix A.3) can be used to rebuild the level set function  $\varphi$ .  
 132 This step is only necessary every 50 to 100 time steps depending on the complexity of the problem and  
 133 the required accuracy.

### 134 3. NUMERICAL RESULTS

135 Our aim in this section is to validate the LSM as an effective method for capturing ice sheet evolution,  
 136 including grounding line migration, by comparing results from numerical simulations against various  
 137 analytical and benchmark solutions. We first compare the LSM result for an idealized glacier test case  
 138 with a prescribed velocity field and mass balance, after which we examine the behavior and performance  
 139 of the LSM for tracking both grounded and marine ice sheet boundaries.

#### 140 3.1. An idealized test case

141 Following Pralong and Funk (2004), we first consider an idealized glacier test case in order to  
 142 focus in on the coupling between the level set calculation and the ice-flow problem. This test case  
 143 fixes the ice flow solution with the given velocity field  $u(x, z) = x^2 + z^2$  and  $w(x, z) = 0$  and glacier  
 144 surface height  $h(x, t) = x - x^2 + xt$ . The corresponding extended mass balance function is chosen as  
 145  $\mathcal{M}(x, z, t) = x + (x^2 + z^2)(1 - 2x + t)$ , so that Eqn (1) is satisfied identically in 2-D (Picasso and others,  
 146 2004). The evolution of this “glacier surface” is then simulated using the level set Eqn (4) with the imposed  
 147 flow field  $u, w$  and mass balance function  $\mathcal{M}(x, z, t)$  so that the evolved surface height may be compared  
 148 with the analytical solution  $h(x, t)$ . The numerical results, from the initial position (at  $t = 0$ ) to the final  
 149 position (at  $t = 2$ ), show excellent agreement with the analytical solution (Fig. 2a). We calculate the  
 150 discrete  $\ell_1$ -norm of the absolute error for  $h$  at  $t = 2$  on uniform spaced grids of  $60 \times 60$ ,  $75 \times 75$ ,  $90 \times 90$   
 151 and  $105 \times 105$  using the second-order TVD-RK and second-order ENO without re-initialization and time  
 152 step  $\Delta t = 0.005$  (Fig. 2b). From these results, we estimate the rate of convergence of the  $\ell_1$  error norm to  
 153 be  $\mathcal{O}(\Delta x^{1.3})$  (and  $\mathcal{O}(\Delta x^{1.9})$  for the  $\ell_2$  error).

#### 154 3.2. Halfar similarity solution

We next apply the level set method to a well-known time-dependent solution of the SIA model called the Halfar similarity solution. To find this exact solution, we first write the no slip SIA equation (Schoof and Hewitt, 2013)

$$\frac{\partial H}{\partial t} = \nabla \cdot (\Gamma H^{n+2} |\nabla h|^{n-1} \nabla h) + \mathcal{M}(\mathbf{x}, t), \quad (6)$$

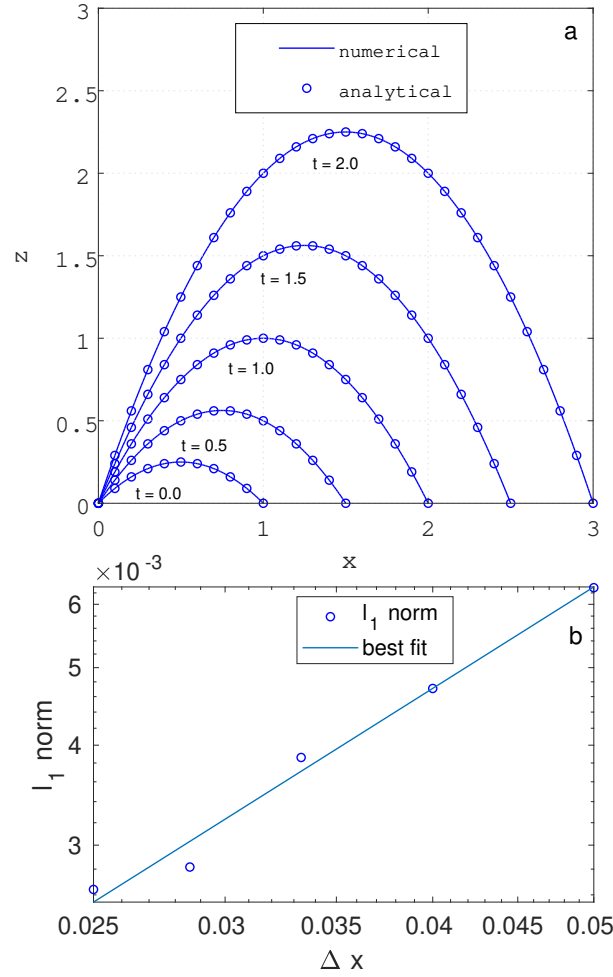


**Fig. 2.** (a) Evolution of the interface due to an imposed velocity field and surface mass balance. The interface position is shown at equally-spaced times between  $t = 0$  and 2. The points ( $\circ$ ) represent the analytical solution and the solid lines correspond to the numerical approximation of the LSM. The simulation uses a spatial grid  $60 \times 60$  and time step  $\Delta t = 0.005$ . (b) Verification of the rate of convergence  $\mathcal{O}(\Delta x^{1.3})$  using the  $\ell_1$ -norm error.

where  $\Gamma = \frac{2A}{n+2}(\rho g)^n$  and  $H$  denotes the ice thickness (refer to Appendix B.1 for details). Halfar (1981) derived a similarity solution for this problem in the case of a flat bed ( $b(\mathbf{x}) = 0$ ) and no surface mass balance ( $\mathcal{M}(\mathbf{x}, t) = 0$ ). Supposing that  $H(0, t_0) = H_0$  for  $t_0 > 0$  and the distance from the origin  $r = (x^2 + y^2)^{1/2}$ , the 2-D Halfar solution to the SIA is

$$H(r, t) = H_0 \left( \frac{t_0}{t} \right)^\alpha \left[ 1 - \left( \left( \frac{t_0}{t} \right)^\beta \frac{r}{R_0} \right)^{\frac{n+1}{n}} \right]^{\frac{n}{2n+1}}, \quad (7)$$

155 where  $t_0 = (\beta/\Gamma)(7/4)^3 R_0^4 H_0^{-7}$  is a characteristic time (Bueler and others, 2005). Note that the values  
 156 of the parameters  $\alpha = \frac{1}{9}$  and  $\beta = \frac{1}{18}$  are such that the factors  $t^{-\alpha}$  and  $t^{-\beta}$  change very slowly for large  
 157 times  $t$ . Other parameters used in this computation are the Glen's flow law exponent  $n = 3$  and ice softness



158  $A = 10^{-16} \text{ Pa}^{-3} \text{ a}^{-1}$ , ice density  $\rho = 910 \text{ kg m}^{-3}$ , gravitational acceleration  $g = 9.81 \text{ m s}^{-2}$ ,  $H_0 = 3600 \text{ m}$ ,  
 159 and  $R_0 = 750 \text{ km}$ .

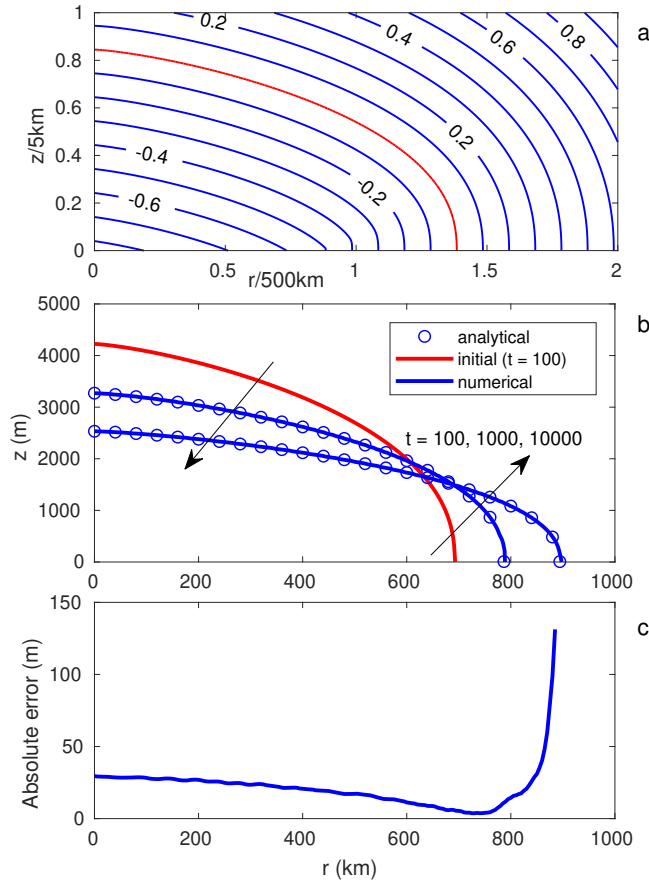


**Fig. 3.** (a) A contour plot of the initial level set function  $\varphi$  at  $t = 100$  with the red line denoting the zero level set,  $\varphi = 0$ , of the ice surface; (b) surface elevations of the evolving ice sheet; (c) the absolute error between the Halfar exact solution and the computed LSM solution at  $t = 10000$  years.

160 We choose initial time  $t = 100$  in Eqn (7) so that  $H(r, t = 100)$  is the initial ice thickness. To compute the  
 161 surface elevation of the Halfar similarity solution using the LSM, we evolve the level set Eqn (4) with the  
 162 SIA horizontal and vertical velocities (Eqns (B8) and (B9), respectively) to compute the new surface at time  
 163  $t$ , identified with  $\varphi(r, z, t) = 0$ . The level set function is computed on the domain  $[0, 1000] \text{ km} \times [0, 5000] \text{ m}$   
 164 with  $200 \times 100$  grid size ( $\Delta r = 5 \text{ km}$  along the radial axis and  $\Delta z = 50 \text{ m}$  along the vertical axis).

165 We compute an extended velocity field outside the ice, which is then used to generate a signed distance  
 166 function (Eqn (3)) depicted in Fig. 3a based on the initial level set function  $\varphi(r, z, t = 100)$ . This initial  
 167 surface is then evolved in time and Fig. 3b compares the surface elevation of the ice sheet at  $t = 1000$  and  
 168  $10000$  years (where  $\varphi(r, z, 1000) = 0$  and  $\varphi(r, z, 10000) = 0$ ) with the Halfar solution (Eqn (7)). The absolute  
 169 error between the elevations from the exact Halfar solution and the LSM approximation at  $t = 10000$  years

170 is small, limited to at most 30 m at the ice divide (Fig. 3c). The error increases toward the margin due to  
 171 steeper surface gradients near the terminus (Fig. 3c). In spite of this, the position of the margin is obtained  
 172 to within a relative error of 0.29% (comparing 894.14 km (Halfar) with 896.71 km (LSM)). These results  
 173 are in close agreement with the exact solution. We repeated the experiment with uniformly spaced grids  
 174 of  $160 \times 80$ ,  $200 \times 100$ ,  $250 \times 125$  and  $300 \times 150$  and found the rate of convergence of the absolute error in  
 175 the position of the margin to be  $\mathcal{O}(\Delta r^{1.1})$ .

### 176 3.3. Radially symmetric ice sheet experiments

177 In this section we perform a moving-margin experiment described in the European Ice Sheet Modelling  
 178 INiTiative (EISMINT) intercomparison project (Huybrechts and Payne, 1996). The aim of this experiment  
 179 is to find a steady state ice sheet surface solution for a given mass balance function.

Before addressing the EISMINT experiment we first introduce the steady state solution for an ice sheet with flat bedrock which occurs when the net mass of ice remains constant over some period of time. In other words, the rate of change of the ice thickness  $\frac{\partial H}{\partial t} = 0$ , so that the SIA mass balance (Eqn (6)) reduces at steady state to

$$\mathcal{M}(r) - \frac{1}{r} \frac{\partial(rH\bar{u})}{\partial r} = 0, \quad (8)$$

where  $r$  is the radial coordinate and  $\bar{u}$  is the vertically averaged ice velocity. Assuming that the surface mass balance  $\mathcal{M}(r)$  is independent of time and the bedrock is flat, the solution for the steady ice thickness profile is

$$H(r) = \left( \left( \frac{2(n+1)}{n\rho g} \right)^n \frac{n+2}{2A} \right)^{\frac{1}{2(n+1)}} \times \left( \int_r^R \left( \frac{1}{\xi} \int_0^\xi \mathcal{M}(\eta)\eta d\eta \right)^{\frac{1}{n}} d\xi \right)^{\frac{n}{2(n+1)}}, \quad (9)$$

where  $R$  denotes the margin position at steady state (Bonan and others, 2016). The EISMINT intercomparison project imposes the surface mass balance function

$$\mathcal{M}(r) = \min(0.5, 10^{-2} \cdot (450 - r)) \text{ m a}^{-1}, \quad (10)$$

180 for which the bisection method (a simple numerical root-finding algorithm) can be applied to  
 181  $\int_0^R \mathcal{M}(\eta)\eta d\eta = 0$  to find the steady state margin position of  $R = 579.81$  km. We note that the integral  
 182  $\int_0^\xi \mathcal{M}(\eta)\eta d\eta$  in Eqn (9) can be evaluated numerically using (Eqn (10)), and so the steady  $H$  profile can  
 183 be estimated accurately using Simpsons 1/3 rule (see Bonan and others, 2016). Parameters used in the

184 EISMINT benchmarks are the Glen's flow law exponent  $n = 3$  and ice softness  $A = 10^{-16} \text{ Pa}^{-3} \text{ a}^{-1}$ , ice  
 185 density  $\rho = 910 \text{ kg m}^{-3}$ , and gravitational acceleration  $g = 9.81 \text{ m s}^{-2}$ .

We perform two experiments on a flat bedrock with no sliding. The first is the EISMINT moving margin experiment, designed with no initial ice mass (Huybrechts and Payne, 1996). The second is similar but initialized with the following ice mass profile (Bonan and others, 2016):

$$H_0(r) = 1000 \left( 1 - \left( \frac{r}{450} \right)^2 \right) \text{ m.} \quad (11)$$

Figures 4a and 4b depict the evolution of the ice sheet geometry for these two initial conditions and both

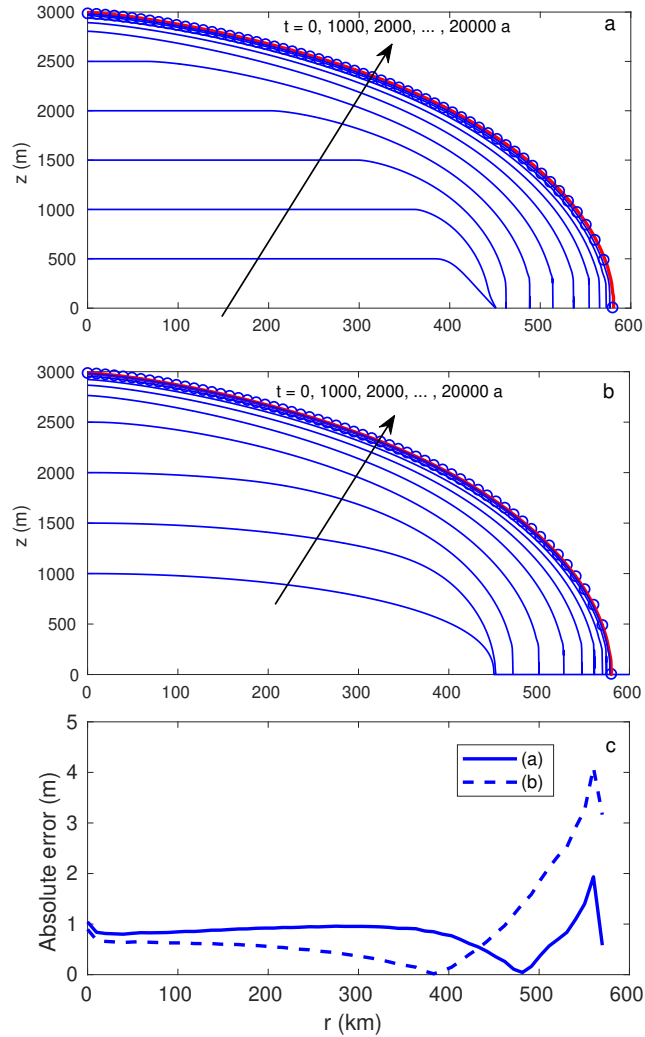


**Fig. 4.** Ice surface solutions for the EISMINT moving-margin experiment with (a) zero initial ice mass and (b) initial ice mass given by Eqn (11). The LSM simulated profiles are shown every 1000 years (blue lines) until steady state at  $t = 20000$  years (red line) and the steady state reference solution is represented by circles. (c) The absolute error at the steady state between the LSM (without and with an initial ice mass) and the numerical reference value.

**Table 1.** Steady state results from the EISMINT moving-margin experiment. A comparison between the benchmark solutions (see Table 5 in Huybrechts and Payne, 1996), the reference solution from numerical integration using Eqn (9), and the LSM solutions with grid size  $240 \times 60$  ( $\Delta r = 2.7$  km and  $\Delta z = 60$  m) obtained without an initial ice mass and with an initial ice mass from Eqn (11).

	Ice thickness at $r = 0$ (in m)	Position of the margin (in km)
EISMINT/2d	$2982.3 \pm 26.4$	$593.3 \pm 9.0$
Reference	2986.91	579.81
LSM (without initial ice mass)	2987.96	579.96
LSM (with initial ice mass)	2987.81	579.94

186

187 are run for 20,000 years to reach the steady state. The steady state ice divide thickness was found to be  
 188 2986.91 m and 2987.81 m for the two experiments, which both lie within the range  $2982.3 \pm 26.4$  m given by  
 189 the EISMINT intercomparison, and are extremely close to the numerically integrated value obtained from  
 190 Eqn (9) (Table 1). Similarly, the margin position of both experiments are very close to the numerically  
 191 integrated reference value in Table 1. The absolute error between the simulated result and the reference ice  
 192 thickness across the profile is mostly less than 1 m and never rises above 4.1 m (Fig. 4c). The relative  $\ell_1$ -  
 193 norm errors of the surface elevation with and without initial ice mass experiments are 0.038% and 0.036%,  
 194 respectively. After repeating the experiment, without initial ice mass, for grid sizes  $192 \times 60$ ,  $216 \times 60$ ,  
 195  $240 \times 60$  and  $264 \times 60$  we determined the rate of convergence of the absolute error in the position of the  
 196 margin to be  $\mathcal{O}(\Delta r^{1.5})$ . Both Table 1 and Fig. 4 show that our LSM method is able to achieve an excellent  
 197 equivalent estimation of the EISMINT intercomparison result without using coordinate stretching or grid  
 198 refinement near the terminus.

We now investigate two further experiments, following Bonan and others (2016), which use the EISMINT surface mass balance with no initial ice mass and a non-flat (fixed) bedrock elevation

$$b(r) = 2000 - 2000 \left(\frac{r}{300}\right)^2 + 1000 \left(\frac{r}{300}\right)^4 - 150 \left(\frac{r}{300}\right)^6 \text{ m.} \quad (12)$$

199 The first experiment considers no sliding, and the second includes sliding with a bed friction parameter  
 200  $C = 7.624 \times 10^6 \text{ Pa s}^{1/3} \text{ m}^{-1/3}$ . Ice sheet profiles for these non-flat bedrock experiments reach a steady state

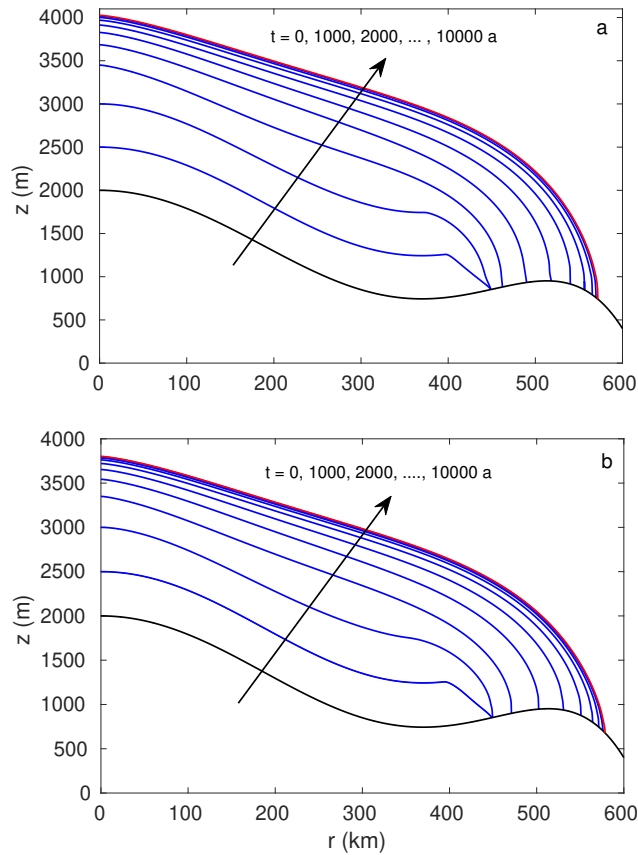


**Fig. 5.** Ice surface solutions for the EISMINT moving-margin experiment with non-flat bedrock (a) without basal sliding and (b) with basal sliding. The LSM simulated profiles are shown every 1000 years (blue lines) until steady state at  $t = 10000$  years (red line). The grid size is  $240 \times 60$  ( $\Delta r = 2.5$  km and  $\Delta z = 50$  m).

201 by roughly  $t = 10000$  years (see Fig. 5). The ice divide thickness at steady state was found to be 4026.25 m  
 202 for the non-sliding case and 3801.72 m for the sliding case. The margin position of the non-sliding and  
 203 sliding experiments are 571.81 km and 578.47 km, respectively. We have found that the LSM produces  
 204 smooth changes along the ice interface in contrast to the moving-point approach of Bonan and others  
 205 (2016) which show linear gradients of the ice sheet surface near the margin as a result of the mesh size  
 206 (refer to Figures 2 and 4 from Bonan and others (2016)). This is because our ice interface is determined  
 207 with sub-grid scale accuracy as we interpolate between the 2-D level set values to determine the zero level  
 208 set, whereas the ice interface in Bonan and others (2016) is linearly interpolated between the 1-D grid  
 209 points of the ice thickness evolution equation.

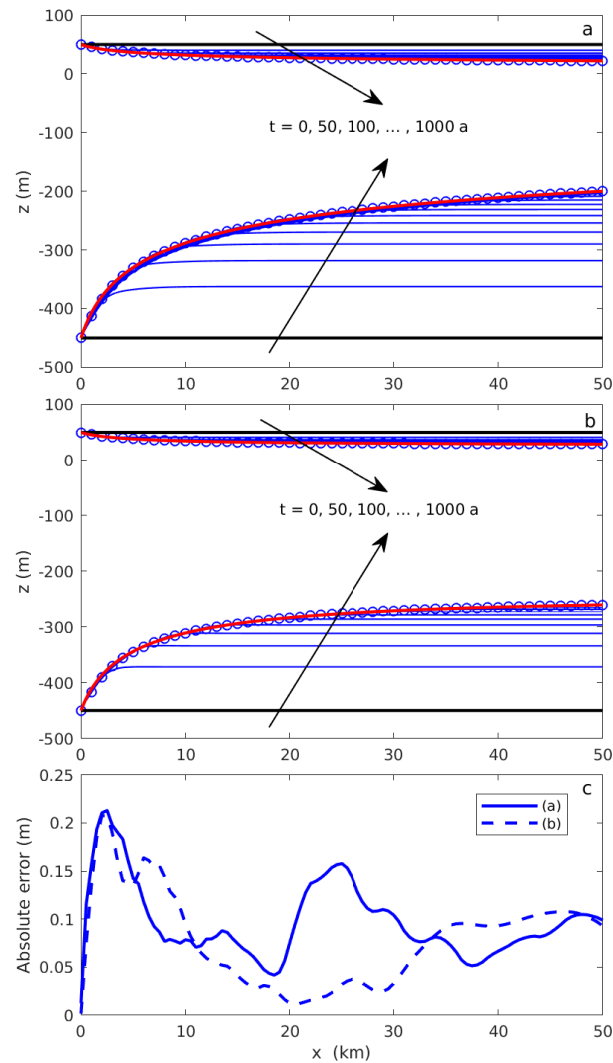


**Fig. 6.** Evolution of the ice shelf interface using the shallow shelf approximation for cases (a) zero accumulation and (b) accumulation  $\mathcal{M} = 0.3 \text{ m a}^{-1}$ . The initial shelf is a rectangular block of ice and the interface is displayed every 50 years, with the steady state highlighted in red. The points ( $\circ$ ) show the exact ice shelf solution for comparison. (c) Absolute error of the steady state ( $t = 1000$  years) for both experiments.

### 210 3.4. Marine ice sheet experiments

211 For the remainder, we shift our focus to simulating marine ice sheets using the governing equations for the  
 212 shallow shelf approximation (SSA) described in Appendix B.2.

#### 213 3.4.1. Steady ice shelf

214 The velocity and thickness of a steady 1-D marine ice shelf can be computed analytically due to the relative  
 215 simplicity of the SSA Eqn (B12) (Van der Veen, 1983). The exact solution depends on the velocity and  
 216 ice thickness at the grounding line, which we take to be  $u_g = 50 \text{ m a}^{-1}$  and  $H_g = 500 \text{ m}$  respectively. We

217 propose two experiments, one where the surface mass balance  $\mathcal{M} = 0$  and a second with  $\mathcal{M} = 0.3 \text{ m a}^{-1}$ . In  
 218 both cases, the initial condition is an ice shelf block having dimensions  $[0, 50] \text{ km} \times \left[ \frac{\rho}{\rho_w} H_g, \left( \frac{\rho}{\rho_w} - 1 \right) H_g \right] \text{ m}$ ,  
 219 which satisfies the flotation criteria. The bottom boundary is considered a free surface in the water without  
 220 any basal melting. The horizontal velocity is computed using the Picard iteration (B16) and then the  
 221 vertical velocity is determined using Eqn (B15). The grid spacings for the LSM solver are  $\Delta x = 0.5 \text{ km}$   
 222 and  $\Delta z = 5 \text{ m}$  with the same grid spacing  $\Delta x_v = 0.5 \text{ km}$  used for the velocity solver. The ice surface is  
 223 evolved in time using the LSM (Eqn (4)) and Figs. 6a and 6b depict the surface profiles at various times for  
 224 the two experiments with and without accumulation. The steady-state ice thickness at  $x = 50 \text{ km}$  for the  
 225 case without accumulation is found to be  $223.14 \text{ m}$  and with accumulation ( $\mathcal{M} = 0.3 \text{ m a}^{-1}$ ) is  $290.73 \text{ m}$ .  
 226 The absolute error is slightly higher near the grounding line as expected due to the steeper ice thickness  
 227 gradient at this location (Fig. 6c). The relative  $\ell_1$ -norm errors in the ice-air shelf interface with and without  
 228 accumulation are  $0.24\%$  and  $0.34\%$ , respectively and the rates of convergence using the  $\ell_1$ -norm error are  
 229  $\mathcal{O}(\Delta x^{1.1})$  and  $\mathcal{O}(\Delta x^{1.3})$ , respectively. These numerical results show very good agreement with the exact  
 230 steady state solution for these ice shelf test cases.

**Table 2.** Parameter values the marine ice sheet experiments.

Parameter	Value
ice density, $\rho$	$900 \text{ kg m}^{-3}$
water density, $\rho_w$	$1000 \text{ kg m}^{-3}$
gravitational acceleration, $g$	$9.8 \text{ m s}^{-2}$
exponent in Glen's law, $n$	3
surface mass balance, $\mathcal{M}$	$0.3 \text{ m a}^{-1}$
bed friction exponent, $m$	$1/3$
bed friction parameter, $C$	$7.624 \times 10^6 \text{ Pa.s}^{1/3} \text{ m}^{-1/3}$

### 231 3.4.2. Marine ice sheet benchmark experiment

Our final experiment is a study of the full marine ice sheet that includes a grounded ice stream attached  
 to a floating ice shelf. The goal here is to examine the ability of the LSM to accurately track grounding  
 line migration. We will study the hysteresis effect for a two-dimensional symmetrical marine ice sheet and  
 compare results with the benchmark Experiment 3 (EXP 3) from the Marine Ice Sheet Intercomparison

Project (MISMIP)(Pattyn and others, 2012). The setup uses an overdeepened bed with polynomial shape

$$b(x) = 729 - 2184.8 \left(\frac{x}{750}\right)^2 + 1031.72 \left(\frac{x}{750}\right)^4 - 151.72 \left(\frac{x}{750}\right)^6 \quad \text{m}, \quad (13)$$

232 and model parameter values given in Table 2. The experiment consists of a sequence of 13 steps (or time  
 233 intervals) of a given length, in each of which the ice sheet has a different value of the Glen’s flow rate  
 234 constant  $A$  (the data is summarized in Table 3). Horizontal and vertical grid spacings for the level set  
 235 discretization are  $\Delta x = 7.5$  km and  $\Delta z = 60$  m. To ensure a sufficiently accurate horizontal velocity we use  
 236 a finer grid for the velocity solver with spacing  $\Delta x_v = 1.875$  km, although only velocities coincident with  
 237 the level set grid are used by the level set solver. We use a time step of  $\Delta t = 5$  years and every 500 years  
 238 the level set function is re-computed using the fast marching method (see Appendix A.3). The solution  
 239 is initialized with a 50 m thick grounded ice layer that extends to the location where it becomes afloat at  
 240 position  $x = 479.1$  km.

**Table 3.** Values of the Glen’s flow law rate constant  $A$  and time intervals used for each step of the MISMIP EXP 3 benchmark, corresponding to the simulations displayed in Fig. 7 (Pattyn and others, 2012).

Step no.	$A$ ( $\text{s}^{-1}\text{Pa}^{-3}$ )	time interval (years)
1	$3 \times 10^{-25}$	$3 \times 10^4$
2	$2.5 \times 10^{-25}$	$1.5 \times 10^4$
3	$2 \times 10^{-25}$	$1.5 \times 10^4$
4	$1.5 \times 10^{-25}$	$1.5 \times 10^4$
5	$1 \times 10^{-25}$	$1.5 \times 10^4$
6	$5 \times 10^{-26}$	$3 \times 10^4$
7	$2.5 \times 10^{-26}$	$3 \times 10^4$
8	$5 \times 10^{-26}$	$1.5 \times 10^4$
9	$1 \times 10^{-25}$	$1.5 \times 10^4$
10	$1.5 \times 10^{-25}$	$3 \times 10^4$
11	$2 \times 10^{-25}$	$3 \times 10^4$
12	$2.5 \times 10^{-25}$	$3 \times 10^4$
13	$3 \times 10^{-25}$	$1.5 \times 10^4$

241 The model simulation proceeds as follows. Starting from the initial values, the solution is computed  
 242 using the value of  $A$  listed for step 1 in Table 3 and over the corresponding time interval. The code is then



243 restarted with the new value of  $A$  listed in step 2 and using the result from the first step as the initial  
 244 state. This procedure continues until the end of the final step and the results are shown in Fig. 7. The

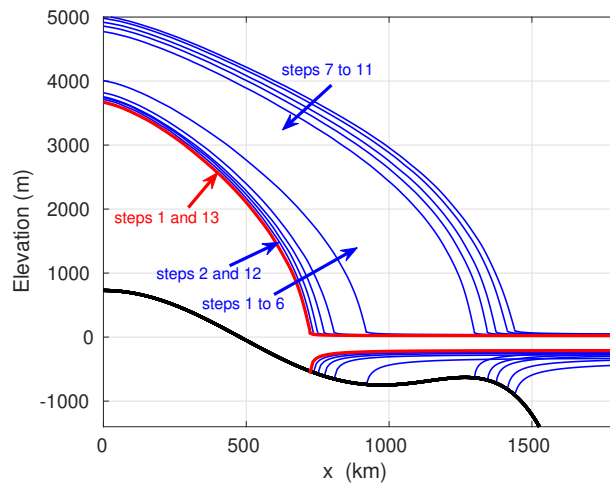


**Fig. 7.** Simulated steady state profiles of the MISIMIP EXP 3 results. Steps 1–13 correspond to the parameter changes listed in Table 3.

244

245 corresponding grounding line (GRL) position is plotted as a function of  $1/A$  in Fig. 8 in order to demonstrate  
 246 the hysteresis phenomenon and compare with the MISIMIP results in Fig. 5 of Pattyn and others (2012).

247 In Fig. 8 the black S-shaped curve represents the path according to the boundary layer theory of Schoof

248 (2007) with our modelled steady state grounding line positions correctly located on the upper and lower

249 branches of this approximate analytic solution. The SSA fixed grid models used in MISIMIP EXP 3 (EBU1

250 ( $\Delta x = 6$  km), DPO4 ( $\Delta x = 0.1$  km), and FPA5 ( $\Delta x = 0.3$  km)) are either unable to reproduce hysteresis or

251 have solutions which lie several tens of kilometres from the boundary layer theory (see red plots in Fig. 8).

252 In contrast, our lower resolution fixed-grid ( $\Delta x = 7.5$  km) level-set approach produces modelled positions

253 that closely match those only achieved with the highly resolved ( $\Delta x \leq 1.2$  km) moving grid methods or

254 the finest adaptive grid ( $\Delta x = 0.15$  km) SSA models in the MISIMIP (see Fig. 5 and Table 2 in Pattyn

255 and others (2012)). Our results in Fig. 8 are also plotted with SSA-H FPA4 ( $\Delta x = 1.2$  km), a MISIMIP

256 participating SSA model with the Pollard and DeConto heuristic (a grounding line parameterization that

257 uses the matched asymptotics of Schoof (2007)) and show excellent agreement (Pattyn and others (2012)).

258 Another test of the numerical results is to compare the difference in GRL position between steps 2 and 12,

259 where any differences are expected to be a result of numerical approximation (Durand and others, 2009a).

260 For our LSM configuration we calculate this gap to be 3.17 km (2.13 km between steps 1 and 13) using our

261 relatively coarse uniform grid ( $\Delta x = 7.5$  km for the LSM and  $\Delta x_v = 1.875$  km for the velocity solver). We

262 note that in Figure 6 of Durand and others (2009a) the grid size has to be as low as 40 m to achieve a similar  
 263 degree of accuracy and a mesh size of 25 – 200 m close to the grounding line was used by Gagliardini and  
 264 others (2016); however, these are full Stokes models and so use a different physical approximation needing  
 higher resolution.

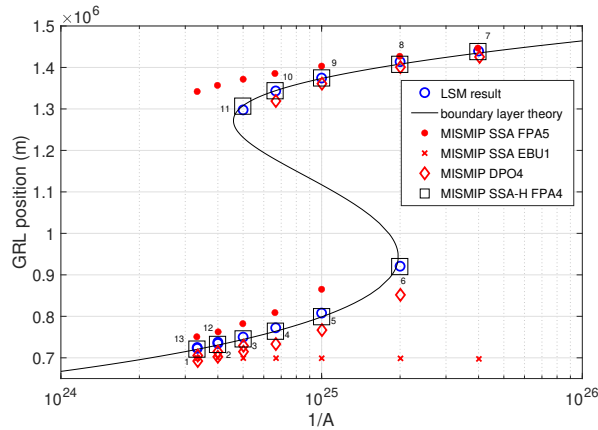


**Fig. 8.** Hysteresis in the grounding line position as a function of forcing viscosity ( $A^{-1}$ ) for MISMIP EXP 3. The black line is from the boundary layer theory of Schoof (2007); ‘ $\circ$ ’ points represent results from our LSM simulations; the red points ‘ $\bullet$ ’, ‘ $\times$ ’, and ‘ $\diamond$ ’ depict results from the fixed grid MISMIP participating models SSA FPA5, SSA EBU1, and SSA DPO4, respectively; and ‘ $\square$ ’ points are from the MISMIP participating model SSH-H FPA4 which uses the Pollard and DeConto heuristic (see Fig. 5 in Pattyn and others (2012)).

265

266 To investigate further we examine the sensitivity of the GRL position ( $x_g$ ) of the steady state ice sheet  
 267 profiles between steps 2 and 12 for different mesh resolution. For this reason, we compare results using  
 268 a grid size of  $(\Delta x, \Delta z) = (10 \text{ km}, 80 \text{ m}), (7.5 \text{ km}, 60 \text{ m}), (5 \text{ km}, 40 \text{ m})$  and  $(3.75 \text{ km}, 30 \text{ m})$  for the LSM with  
 269 a fixed grid size  $\Delta x_v = 15/8 \text{ km}$  for the velocity solver. Similarly, we also consider different velocity grid  
 270 sizes with  $\Delta x_v = 15/8, 15/16, 15/32,$  and  $15/64 \text{ km}$  and a fixed grid size  $(\Delta x, \Delta z) = (3.75 \text{ km}, 30 \text{ m})$  for  
 271 the LSM. Results are presented in Fig. 9a and Fig. 9b where steady  $x_g$  are plotted as a function of the  
 272 horizontal grid size  $\Delta x$  of the LSM and the grid size  $\Delta x_v$  of the velocity solver, respectively. In Fig. 9a,  
 273 the GRL position gap between steps 2 and 12 reduces as the grid size is reduced and reaches 1.89 km at  
 274 the LSM grid  $\Delta x = 3.75 \text{ km}$ . Numerical results also depend on the accuracy of velocities that we use for  
 275 the LSM. When steady  $x_g$  are presented as a function of the grid size of the velocity solver (for a fixed  
 276 LSM grid size  $\Delta x = 1.875 \text{ km}$ ) the gap reduces to 150 m and we find that the GRL converges to a value  
 277 near 730 km at the lowest resolution (Fig. 9b).

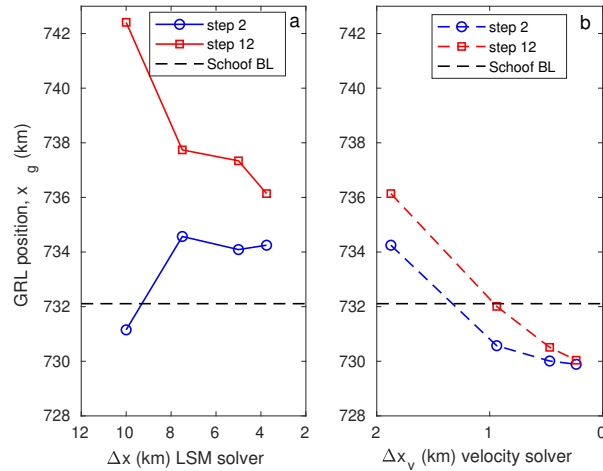


**Fig. 9.** Evolution of the steady  $x_g$  as a function of (a) the horizontal mesh size  $\Delta x$  of the LSM for fixed mesh size  $\Delta x_v = 1.875$  km of the velocity solver and (b) the mesh size  $\Delta x_v$  of the velocity solver for fixed mesh size  $\Delta x = 3.75$  km of the LSM. Blue circles (red squares) represent results obtained for simulations starting from the steady state obtained at step 2 (step 12). The dashed line depicts results obtained using Schoof's boundary layer (BL) theory reported in Durand and others (2009a).

278 We have shown that by using the LSM on a relatively coarse fixed grid we can determine the evolving  
 279 grounding line position with fine-scale accuracy. The zero level set determines the ice interface and is found  
 280 by interpolating level set values computed on the fixed grid. The grounding line position is identified as  
 281 the location where the zero level set meets the bottom of the domain. In spite of our coarse grid this  
 282 method allows us to determine the grounding line position with subgrid scale precision. The LSM requires  
 283 an additional dimension and therefore greater computational time is needed compared to solving the  
 284 kinematic boundary condition (Eqn (1)). This additional computational time cost is especially apparent  
 285 when solving the relatively fast SIA and SSA, but would not be so significant if the LSM were coupled to the  
 286 more computationally demanding full-Stokes equations. Regardless, simulating grounding line migration  
 287 has required ice sheet models using irregular and adaptive mesh refinements, which come with considerable  
 288 computational cost and complexity, whereas we have shown that a regular fixed-grid model, using the  
 289 LSM, can accurately track advancing and retreating grounding line positions. Furthermore, the coarser  
 290 grid also results in computational savings from the longer time steps allowed by the CFL condition. The  
 291 other alternative is to use a subgrid parameterization, such as using a heuristic rule based on boundary  
 292 layer theory valid for steady-states. The level-set approach used here does not rely on a parameterization  
 293 or employ any other special treatment at the grounding line. The method described has not been tried

294 for two horizontal dimensions, but the 3D LSM could be implemented by extending the array structures  
295 and gradient operators for tracking the propagating surfaces in two horizontal dimensions (Sethian, 1999b;  
296 Bondzio and others, 2016).

## 297 4. CONCLUSIONS

298 We have devised a new level set algorithm for tracking an evolving ice sheet surface and grounding line  
299 position, based on an underlying fixed-grid finite difference discretization. Other fixed-grid methods tend  
300 to be less competitive relative to moving grid methods for dynamic interface problems like ice sheet models,  
301 and they can only obtain comparable accuracy with moving-grid methods by using highly resolved grids  
302 near the grounding line. Our level-set approach is able to track the ice sheet margin and grounding line  
303 location dynamically for both grounded and marine ice sheets without the need for grid refinement and  
304 any subgrid parameterization or heuristic rule. The method is tested by comparing numerical simulations  
305 with analytical and benchmark solutions. In particular, we compared model solutions for grounded ice  
306 sheets with the EISMINT benchmark (Huybrechts and Payne, 1996) and for marine ice sheets with the  
307 MISMIP intercomparison benchmark (Pattyn and others, 2012). These experiments demonstrate that the  
308 level set method is an accurate approach for capturing the ice sheet marginal position, while exploiting the  
309 efficiency in using an underlying fixed grid that is coarse relative to other methods that employ a uniformly  
310 or locally adapted fine mesh. We have therefore shown that the level set method is an accurate and efficient  
311 approach for tracking the ice surface interface, terminus positions and grounding lines for grounded and  
312 marine ice sheets.

## 313 5. ACKNOWLEDGEMENTS

314 We gratefully appreciate the clear and detailed feedback from the anonymous reviewers and the Scientific  
315 Editor Ian Hewitt. This work has been supported by a Natural Sciences and Engineering Research Council  
316 (NSERC) Discovery Grant.

## 317 APPENDIX A. NUMERICAL IMPLEMENTATION OF THE LSM

### 318 A.1. Extended speed

The level set equation (4) requires that the speed  $F$  (Eqn (5)) is defined for all level sets throughout the computational domain  $\Omega$ , not just the zero level set or on one side of the interface. Firstly, the mass balance source term is prescribed on the interface only and must be smoothly extended within the ice for numerical

stability. As such  $\mathbf{M}$  is determined by linearly interpolating vertically between  $\mathcal{M}_h$  on the ice-air interface and  $\mathcal{M}_b$  on the ice-water (or ice-bedrock) interface. Note, that this is an artificial measure that helps to smooth the derivatives in the level set method solver and not a real change in ice mass. In our case the ice velocity components are obtained from an ice sheet model and thus defined inside the ice region ( $\Omega_i$ ). Hence, these velocities, added to  $\mathbf{M}$ , must now be extended outside the ice domain ( $\Omega_c$ ) (Adalsteinsson and Sethian, 1999). Given a level set function  $\varphi$ , our goal is then to construct the extended speed  $F^{\text{ext}}$  such that

$$\frac{\partial \varphi}{\partial t} + F^{\text{ext}} \|\nabla \varphi\| = 0, \quad (\text{A1})$$

where we require that  $F^{\text{ext}}$  matches the given speed  $F$  on the zero level set,

$$F^{\text{ext}} = F \quad \text{on} \quad \varphi(\mathbf{x}(t), t) = 0.$$

This new speed field  $F^{\text{ext}}$  is known as the “extended speed” (see Fig. 10). A desirable feature of  $F^{\text{ext}}$  is

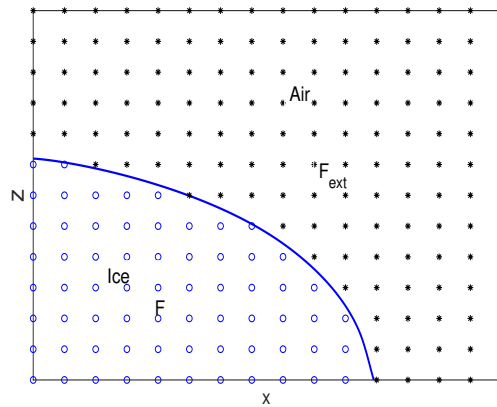


**Fig. 10.** Constructing extended speeds. The solid line inside the domain represents the ice-air interface or zero level set. Suppose  $F$  is known at ‘o’ points inside the ice then  $F^{\text{ext}}$  must be extended to ‘\*’ points outside the ice.

that it should move the neighbouring level sets in such a way that the signed distance function is preserved. Following Zhao and others (1996),  $\varphi(\mathbf{x}(t), t)$  remains a signed distance function if and only if

$$\nabla F^{\text{ext}} \cdot \nabla \varphi = 0, \quad (\text{A2})$$

which in 2-D becomes

$$\frac{\partial \varphi}{\partial x} \frac{\partial F^{\text{ext}}}{\partial x} + \frac{\partial \varphi}{\partial z} \frac{\partial F^{\text{ext}}}{\partial z} = 0. \quad (\text{A3})$$

Since the interface may experience topological changes, a few different cases must be considered when determining  $F^{\text{ext}}$  (Sethian, 1999b). As an example, suppose  $(i-1, j)$  and  $(i, j-1)$  are the points where  $F$  is known (inside the ice), then using finite differences we can approximate the extended speed  $F^{\text{ext}}$  at the position  $(i, j)$  (outside the ice) by

$$F_{i,j}^{\text{ext}} = \frac{F_{i-1,j}(\varphi_{i,j} - \varphi_{i-1,j}) + \left(\frac{\Delta x}{\Delta z}\right)^2 F_{i,j-1}(\varphi_{i,j} - \varphi_{i,j-1})}{(\varphi_{i,j} - \varphi_{i-1,j}) + \left(\frac{\Delta x}{\Delta z}\right)^2 (\varphi_{i,j} - \varphi_{i,j-1})}, \quad (\text{A4})$$

319 where  $\Delta x$  and  $\Delta z$  are the horizontal and vertical grid spacings, respectively. This approach results in  
320 Eqn (A2) being satisfied for all points outside the ice.

## 321 A.2. Numerical scheme

322 The LSM is a versatile numerical technique that can be implemented in concert with a variety of  
323 discretizations including finite differences, finite elements, moving meshes, etc. For the sake of simplicity,  
324 we have chosen to use a fixed, rectangular, Euclidean mesh in which all grid cells are of equal size although  
325 the grid spacing in each direction may be different. After defining discrete values of  $\varphi$  and  $F$  at every grid  
326 point in the computational domain, we use a discrete form of the governing equations to evolve  $\varphi$  forward  
327 in time, and hence transport the interface across the underlying grid.

We use an explicit Runge-Kutta (RK) type scheme to determine  $\varphi(\mathbf{x}, t + \Delta t)$  based on known previous values of  $\varphi(\mathbf{x}, t)$ , the speed in the outward normal direction  $F$ , and the gradient  $\nabla\varphi$ . For a given time,  $t^k$ , let  $\varphi^k = \varphi(t^k)$  and after some time increment  $\Delta t$ , we denote new values as  $\varphi^{k+1} = \varphi(t^k + \Delta t)$ . We implement the Total Variation Diminishing Runge-Kutta (TVD-RK) scheme of second order, also known as Heun's method or the modified Euler method (Osher and Fedkiw, 2006)

$$\varphi_{ij}^{k+1} = \varphi_{ij}^k + \frac{F_{ij}^k \Delta t}{2} \left( \|\nabla\varphi_{ij}^k\| + \|\nabla\tilde{\varphi}_{ij}^{k+1}\| \right), \quad (\text{A5})$$

where

$$\tilde{\varphi}_{ij}^{k+1} = \varphi_{ij}^k + F_{ij}^k \Delta t \|\nabla\varphi_{ij}^k\|,$$

328 and  $\|\nabla\varphi_{ij}\| = \sqrt{((\varphi_x)_{ij})^2 + ((\varphi_z)_{ij})^2}$ . Here  $(\varphi_x)_{ij}$  and  $(\varphi_z)_{ij}$  denote the spatial derivatives of  $\varphi$  at the  
329 position  $(x_i, z_j)$ . As is usual for explicit time-stepping schemes, the allowable time step  $\Delta t$  is restricted in  
330 practice by a Courant-Friedrichs-Lewy (CFL) condition that depends on the spatial grid size  $\Delta x$  and the  
331 flow speed.

332 Moving on to the spatial discretization, traditional finite difference methods based on fixed stencil  
333 interpolations work well for globally smooth problems, but at second or higher order spatial accuracy

334 these schemes are necessarily oscillatory near a discontinuity. We therefore approximate spatial derivatives  
 335  $(\varphi_x)_{ij}$  and  $(\varphi_z)_{ij}$  in Eqn (A5) using the Essentially Non-Oscillatory (ENO) scheme (Osher and Fedkiw,  
 336 2006). In this approach, a higher order non-oscillatory interpolant for piecewise smooth functions is used  
 337 to approximate  $\varphi$ , and is then differentiated piecewise to obtain a corresponding discrete approximation  
 338 for  $\nabla\varphi$ . In essence, the ENO approach extends first-order accurate upwind differencing to second-order  
 339 spatial accuracy in a way that suppresses oscillations.

340 We next discuss suitable choices for initial and boundary values of  $\varphi$ . The level set function can be  
 341 initialized simply using Eqn (3) with  $\partial\Omega$  as the initial surface for the ice sheet. Then, using the extended  
 342 velocity discussed in Section A.1, the level set in every subsequent time step is guaranteed to remain a  
 343 signed distance function.

Every node at the edge of the computational domain must be assigned a suitable boundary condition. We  
 choose to use a special form of linear extrapolation described by Mitchell (2004) that adds an appropriate  
 number of “ghost nodes” beyond the edge of the grid when working on nodes near the edge. The values  
 of  $\varphi$  at ghost nodes are determined by linear extrapolation from the computational boundary with a slope  
 direction that matches the sign of the level set at the boundary node. Suppose  $(x_i, z_j)$  for  $i = 1, 2, \dots, p$   
 and  $j = 1, 2, \dots, q$  are nodes in the domain and  $(x_0, z_j)$ ,  $(x_{p+1}, z_j)$ ,  $(x_i, z_0)$  and  $(x_i, z_{q+1})$  are ghost nodes,  
 then the values at the ghost nodes left of the domain are given by

$$\varphi(x_0, z_j) = \varphi(x_1, z_j) + \text{sign}(\varphi(x_1, z_j))|\varphi(x_1, z_j) - \varphi(x_2, z_j)|,$$

344 for  $j = 1, 2, \dots, q$ , and we similarly define the values at the other ghost nodes  $(x_{p+1}, z_j)$ ,  $(x_i, z_0)$  and  
 345  $(x_i, z_{q+1})$ . This is not a traditional PDE boundary condition, however, it is quite useful in level set  
 346 computations for domains with inflow boundaries that have no physically appropriate boundary conditions,  
 347 as it remains stable whereas regular linear extrapolation may cause stability issues (Mitchell, 2004).

### 348 **A.3. Re-initialization using the Fast Marching Method**

349 The level sets that are located near the zero level set move with speeds that can considerably distort  
 350 and stretch the level set function  $\varphi$ . Under such circumstances,  $\varphi$  can develop noisy features and steep  
 351 gradients that are detrimental to finite-difference approximations and so can fail to preserve the signed  
 352 distance function. As a result, it may be necessary to periodically re-initialize the level set function, which  
 353 involves stopping the calculation at some point in time and rebuilding the level set function according to

354 the signed distance function (Sethian, 1999b), thereby ensuring that  $\varphi$  remains smooth enough to allow its  
355 spatial derivatives to be computed with sufficient accuracy.

356 Although there are several ways this re-initialization could be carried out in practice, we implement the  
357 Fast Marching Method (FMM), which is known to be very effective for this purpose. The FMM offers a fast  
358 approach for rebuilding  $\varphi$  having computational cost of  $\mathcal{O}(N \log N)$ , where  $N$  is the total number of grid  
359 points (Adalsteinsson and Sethian, 1999). To re-initialize the signed distance function  $\varphi$ , the FMM solves  
360 the eikonal equation  $\|\nabla\varphi\| = 1$  on either side of the interface  $\partial\Omega$  (Sethian, 1999a; Vogl, 2016). The FMM  
361 algorithm considers three categories of grid points: CLOSE, FAR and ACCEPTED. The ACCEPTED  
362 points are initially assigned to grid nodes that immediately surround the zero level set, CLOSE points are  
363 then one grid point further away, and the remaining nodes in the domain are labelled FAR (see Fig. 11).  
364 The shortest path from each ACCEPTED grid node to the contour of the zero level set (ice-air or ice-  
365 water interface) is determined using a non-linear optimization solver and used to assign the signed-distance  
366 value to each ACCEPTED point. The procedure continues with the following steps that efficiently and  
367 systematically marches CLOSE and FAR points to ACCEPTED in order to assign the signed-distance  
368 value at all grid points in the domain.

- 369 1. The signed-distance value of CLOSE points are calculated based on the known signed-distance at  
370 neighbouring ACCEPTED points and the grid size.
- 371 2. Let TRIAL be the CLOSE point with the smallest value of  $\varphi$ .
- 372 3. Any FAR points that directly neighbour TRIAL are relabelled CLOSE.
- 373 4. Relabel TRIAL points to ACCEPTED.
- 374 5. Repeat steps 1–4 until all points become ACCEPTED.

375 The accuracy of this approach means re-initialization is required less often. For our simulations we used  
376 the FMM to rebuild the level set function every 50 to 100 time steps.



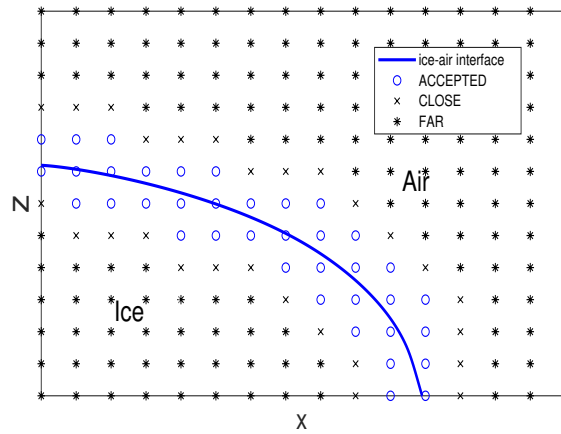


**Fig. 11.** Initialization of the Fast Marching Method, where ‘o’ denote the initial ACCEPTED points, ‘x’ the CLOSE points and ‘\*’ indicating the FAR points.

377 **APPENDIX B. ICE SHEET EQUATIONS**

378 **B.1. Shallow ice approximation (SIA)**

The SIA treats the ice sheet as a shallow film that flows and spreads under its own weight (Hutter, 1983). We denote the sheet thickness at position  $(x, y)$  and time  $t$  by  $H(x, y, t)$ . Then, in terms of  $z$  measured vertically upward from sea level, the height of the upper surface in contact with the atmosphere is represented by  $z = h(x, y, t)$  and the lower bedrock surface by  $z = b(x, y)$  (which has zero normal velocity, assuming negligible melt there). Referring to Fig. 12, these three height variables are related by

$$h(x, y, t) = b(x, y) + H(x, y, t). \tag{B6}$$

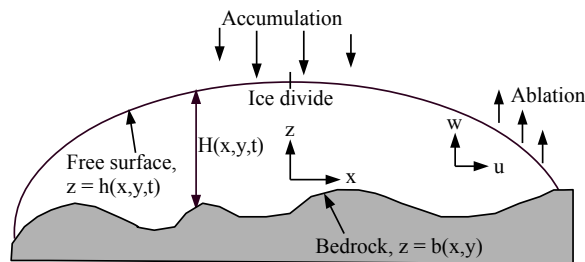


**Fig. 12.** Geometry of the shallow ice sheet flow problem.

379

The ice deformation is determined by the incompressible Stokes equations, coupled with Glen’s flow law (Glen, 1958) under the shallow ice assumption. In the isothermal case, the horizontal velocity

components  $\mathbf{U} = (u, v)$  as

$$\mathbf{U} = -\frac{2A(\rho g)^n}{n+1} [H^{n+1} - (h-z)^{n+1}] |\nabla h|^{n-1} \nabla h, \quad (\text{B7})$$

380 in the case where there is no sliding relative to the underlying bedrock. The other variables and parameters  
 381 in the equations are the gravitational acceleration  $\mathbf{g} = (0, 0, -g)$ , ice density  $\rho$ , creep parameter  $A$ , and  
 382 Glen's law exponent  $n \approx 3$ .

For a grounded ice sheet that is radially symmetric about the ice divide, denoted  $r = 0$ . The radial symmetry implies that the sheet geometry depends only on  $r$  so that  $h = h(r, t)$ ,  $H = H(r, t)$  and  $b = b(r)$ . For the case of non-sliding ice, the radial velocity is  $\mathbf{U} = u \hat{\mathbf{r}}$  where  $\hat{\mathbf{r}}$  denotes the unit vector in the radial direction. At the ice divide ( $r = 0$ ), a symmetry condition is imposed

$$u = 0 \quad \text{and} \quad \frac{\partial h}{\partial r} = 0.$$

To handle the case when there may be some slip at the ice sheet base, we consider a friction law that relates basal stress  $\tau_b$  to the sliding velocity  $u_b$  at the bed by means of the relationship  $\tau_b = f(u_b) = C u_b^1/n$ , where the bed friction parameter  $C$  depends on the local bed roughness and a bed friction exponent,  $m = \frac{1}{n}$  (Schoof and Hewitt, 2013). Using the stress balance and Glen's flow law, the sliding velocity is  $u_b = -\left(\frac{\rho g H}{C} \frac{\partial h}{\partial r}\right)^{1/m}$ , so that the radial velocity can be written in a more general form that captures both the sliding and non-sliding cases:

$$u(r, z, t) = -\frac{2A(\rho g)^n}{n+1} [H^{n+1} - (h-z)^{n+1}] \left| \frac{\partial h}{\partial r} \right|^{n-1} \frac{\partial h}{\partial r} + \begin{cases} 0, & \text{non-sliding,} \\ -\left(\frac{\rho g H}{C} \frac{\partial h}{\partial r}\right)^{1/m}, & \text{sliding.} \end{cases} \quad (\text{B8})$$

The vertical velocity  $w(r, z, t)$  may then be obtained from  $u(r, z, t)$  using the incompressibility condition, which in cylindrical coordinates is

$$\frac{\partial w}{\partial z} + \frac{1}{r} \frac{\partial(ru)}{\partial r} = 0.$$

Integrating this equation in  $z$  and applying the vertical no-flow boundary condition at the bed  $z = b(r)$  yields the corresponding expression for

$$\begin{aligned}
w(r, z, t) = & -\frac{2A}{n+1}(\rho g)^n \left[ \left( \frac{1}{r} \left( \frac{\partial h}{\partial r} \right)^n + n \left( \frac{\partial h}{\partial r} \right)^{n-1} \frac{\partial^2 h}{\partial r^2} \right) \right. \\
& \cdot \left( \frac{1}{n+2} (H^{n+2} - (h-z)^{n+2}) - H^{n+1}(z-b) \right) \\
& \left. + \left( \frac{\partial h}{\partial r} \right)^{n+1} (H^{n+1} - (h-z)^{n+1}) - (n+1) \frac{\partial H}{\partial r} \left( \frac{\partial h}{\partial r} \right)^n H^n (z-b) \right] \\
& + \begin{cases} 0, & \text{non-sliding,} \\ (z-b) \left( \frac{\rho g}{C} \right)^{1/m} \left[ \frac{1}{r} \left( H \frac{\partial h}{\partial r} \right)^{1/m} + \frac{1}{m} \left( H \frac{\partial h}{\partial r} \right)^{\frac{1}{m}-1} \left( H \frac{\partial^2 h}{\partial r^2} + \frac{\partial H}{\partial r} \frac{\partial h}{\partial r} \right) \right], & \text{sliding.} \end{cases} \quad (\text{B9})
\end{aligned}$$

### 383 B.2. Shallow shelf approximation (SSA)

The SSA is used to consider a two-dimensional symmetrical marine ice sheet. Denoting the horizontal coordinate in the flow direction by  $x$ , symmetry implies that

$$u = 0 \quad \text{and} \quad \frac{\partial h}{\partial x} = 0 \quad \text{at} \quad x = 0. \quad (\text{B10})$$

The ice stream or grounded portion of the marine ice sheet occupies the region  $0 \leq x < x_g$ , where  $x_g$  denotes the grounding line position. The momentum conservation equation of SSA for the grounded ice sheet ( $0 \leq x < x_g$ ) was derived by MacAyeal (1989) as

$$\frac{\partial}{\partial x} \left( 2A^{-1/n} H \left| \frac{\partial u}{\partial x} \right|^{1/n-1} \frac{\partial u}{\partial x} \right) - C|u|^{m-1}u = \rho g H \frac{\partial h}{\partial x}, \quad (\text{B11})$$

384 where  $h = b + H$  as in the SIA model,  $C$  is the bed friction parameter and  $H \geq -\frac{\rho_w}{\rho}b$  where  $\rho_w$  is  
385 the sea water density. The SSA Eqn (B11) represents a balance between longitudinal strain rates that  
386 are determined by the integrated ice hardness (the coefficient  $A^{-1/n}H$ ), the slipperiness of the bed (the  
387 coefficient  $C$  and exponent  $m$ ), and the geometry of the ice sheet (the thickness  $H$  and surface slope  $\frac{\partial h}{\partial x}$ ).

For the unbuttressed freely floating ice shelf that occupies the region  $x_g < x < x_c$ , where  $x = x_c$  denotes the calving front, we have  $H < -\frac{\rho_w}{\rho}b$  and  $h = (1 - \rho/\rho_w)H$ . There is no basal friction and so the term  $C|u|^{m-1}u$  vanishes and the sole driving stress for ice shelves is  $\rho(1 - \rho/\rho_w)gH \frac{\partial H}{\partial x}$ , giving the momentum conservation equation for the shelf ( $x_g < x < x_c$ ) as

$$\frac{\partial}{\partial x} \left( 2A^{-1/n} H \left| \frac{\partial u}{\partial x} \right|^{1/n-1} \frac{\partial u}{\partial x} \right) = \rho(1 - \rho/\rho_w)gH \frac{\partial H}{\partial x}. \quad (\text{B12})$$

At the calving front there is an imbalance between hydrostatic pressures in ice and water due to the buoyancy of ice, hence

$$2A^{-1/n}H \left| \frac{\partial u}{\partial x} \right|^{1/n-1} \frac{\partial u}{\partial x} = \frac{1}{2}\rho(1 - \rho/\rho_w)gH^2 \quad \text{at } x = x_c. \quad (\text{B13})$$

388 At the grounding line, where ice stream couples to ice shelf, we have  $H = -\frac{\rho_w}{\rho}b$ , as well as the boundary  
389 condition Eqn (B13) applied at  $x = x_g$ .

Assuming ice to be an incompressible material, the vertical velocity for the ice stream with rigid bedrock ( $\frac{\partial b}{\partial t} = 0$ ) and no melting at the bottom surface is determined by

$$w(x, z, t) = u(x, t) \frac{\partial b}{\partial x} - (z - b(x)) \frac{\partial u}{\partial x}, \quad 0 \leq x \leq x_g. \quad (\text{B14})$$

For the ice shelf the vertical velocity is given by

$$w(x, z, t) = w_{sl} - (z - z_{sl}) \frac{\partial u}{\partial x}, \quad x_g < x \leq x_c, \quad (\text{B15})$$

390 where  $w_{sl}$  is the vertical velocity at sea level that can be determined from the known surface and basal  
391 mass balances,  $\mathcal{M}_h$  and  $\mathcal{M}_b$ , respectively (Greve and Blatter, 2009).

For a given ice thickness  $H(x)$  (determined by the LSM in our case) the velocity  $u(x)$  is determined by solving the nonlinear partial differential equations (B11) and (B12). Our solution approach implements an iterative numerical method, often called a Picard iteration. Denote the current velocity iterate as  $u^{(k)}$  and the previous iterate as  $u^{(k-1)}$ , then the Picard iteration for Eqn (B11) (and similarly for Eqn (B12)) is:

$$\frac{\partial}{\partial x} \left( W^{(k-1)} \frac{\partial u^{(k)}}{\partial x} \right) - C \left| u^{(k-1)} \right|^{m-1} u^{(k)} = \rho g H \frac{\partial h}{\partial x}, \quad (\text{B16})$$

where  $W^{(k-1)} = 2A^{-1/n}H \left| \frac{\partial u^{(k-1)}}{\partial x} \right|^{1/n-1}$ . For grounded ice,  $0 < x < x_g$ , we assume the ice is held by basal resistance only to obtain the initial velocity estimate,  $u^{(0)}(x) = (-C^{-1}\rho g H \frac{\partial h}{\partial x})^{1/m}$  and the boundary conditions from Eqns (B10) and (B13) are  $u(0) = 0$ , and  $\frac{\partial u}{\partial x}(x_g) = A \left( \frac{1}{4}\rho(1 - \rho/\rho_w)gH \right)^n$ . For floating ice,  $x_g < x < x_c$ , an initial guess for velocity comes from assuming a uniform strain rate provided by the calving front condition:

$$u^{(0)}(x) = A \left( \frac{1}{4}\rho(1 - \rho/\rho_w)gH \right)^n (x - x_g) + u_g,$$

392 where  $u_g$  denotes the ice velocity at the grounding line, and the boundary conditions are  $u(x_g) = u_g$  and  
393  $\frac{\partial u}{\partial x}(x_c) = A \left( \frac{1}{4}\rho(1 - \rho/\rho_w)gH \right)^n$ .

## 394 REFERENCES

- 395 Adalsteinsson D and Sethian JA (1999) The fast construction of extension velocities in level set methods. *J. Comput.*  
396 *Phys.*, **148**(1), 2–22 (doi: 10.1006/jcph.1998.6090)
- 397 Bevis M, Harig C, Khan SA, Brown A, Simons FJ, Willis M, Fettweis X, van den Broeke MR, Madsen FB, Kendrick E  
398 and others (2019) Accelerating changes in ice mass within Greenland, and the ice sheet’s sensitivity to atmospheric  
399 forcing. *PNAS*, **116**(6), 1934–1939 (doi: 10.1073/pnas.1806562116)
- 400 Bonan B, Baines MJ, Nichols NK and Partridge D (2016) A moving-point approach to model shallow ice sheets: a  
401 study case with radially symmetrical ice sheets. *Cryosphere*, **10**(1), 1–14 (doi: 10.5194/tc-10-1-2016)
- 402 Bondzio JH, Seroussi H, Morlighem M, Kleiner T, Rückamp M, Humbert A and Larour EY (2016) Modelling calving  
403 front dynamics using a level-set method: application to Jakobshavn Isbræ, West Greenland. *Cryosphere*, **10**(2),  
404 497–510 (doi: 10.5194/tc-10-497-2016)
- 405 Bondzio JH, Morlighem M, Seroussi H, Wood MH and Mouginot J (2018) Control of ocean temperature  
406 on Jakobshavn Isbræ’s present and future mass loss. *Geophys. Res. Lett.*, **45**(12), 12912–12921 (doi:  
407 10.1029/2018GL079827)
- 408 Bueler E, Lingle CS, Kallen-Brown JA, Covey DN and Bowman LN (2005) Exact solutions and verification of  
409 numerical models for isothermal ice sheets. *J. Glaciol.*, **51**(173), 291–306 (doi: 10.3189/172756505781829449)
- 410 Bunce C, Carr JR, Nienow P and Ross N (2018) Ice front change of marine-terminating outlet glaciers in northwest  
411 and southwest Greenland during the 21st century. *J. Glaciol.*, **64**(246), 523–535 (doi: 10.1017/jog.2018.44)
- 412 Caboussat A, Jovet G, Picasso M and Rappaz J (2011) Numerical algorithms for free surface flow. In F Magoules  
413 (ed.), *Computational Fluid Dynamics*, chapter 9, 263–326, CRC Press
- 414 Cornford SL, Martin DF, Graves DT, Ranken DF, Le Brocq AM, Gladstone RM, Payne AJ, Ng EG and Lipscomb  
415 WH (2013) Adaptive mesh, finite volume modeling of marine ice sheets. *J. Comput. Phys.*, **232**, 529–549 (doi:  
416 10.1016/j.jcp.2012.08.037)
- 417 Durand G, Gagliardini O, de Fleurian B, Zwinger T and Le Meur E (2009a) Marine ice sheet dynamics: Hysteresis  
418 and neutral equilibrium. *J Geophys. Res.*, **114**, F03009 (doi: 10.2008JF001170)
- 419 Durand G, Gagliardini O, Zwinger T, Le Meur E and Hindmarsh RCA (2009b) Full stokes modeling of marine ice  
420 sheets: influence of the grid size. *Ann. Glaciol.*, **50**(52), 109–114 (doi: 10.3189/172756409789624283)
- 421 Edwards TL, Brandon MA, Durand G, Edwards NR, Gолledge NR, Holden PB, Nias IJ, Payne AJ, Ritz C and  
422 Wernecke A (2019) Revisiting Antarctic ice loss due to marine ice-cliff instability. *Nature*, **566**, 58–64 (doi:  
423 10.24433/CO.4ebd8cda-35c0-4d8f-9b7c-d1b064109437)

- 424 Gagliardini O, Brondex J, Gillet-Chaulet F, Tavarard L, Peyaud V and Durand G (2016) Brief communication: Impact  
425 of mesh resolution for MISMIP and MISMIP3d experiments using Elmer/Ice. *Cryosphere*, **10**, 307–312 (doi:  
426 10.5194/tc-10-307-2016)
- 427 Gibou F, Fedkiw R and Osher S (2018) A review of level-set methods and some recent applications. *J. Comput.*  
428 *Phys.*, **353**, 82–109 (doi: 10.1016/j.jcp.2017.10.006)
- 429 Glen JW (1958) The flow law of ice: A discussion of the assumptions made in glacier theory, their experimental  
430 foundations and consequences. *International Association of Scientific Hydrology Publication*, **47**, 171–183
- 431 Goldberg DN, Holland DM and Schoof C (2009) Grounding line movement and ice shelf buttressing in marine ice  
432 sheets. *J Geophys. Res.*, **114**, F04026 (doi: 10.1029/2008JF001227)
- 433 Greve R and Blatter H (2009) *Dynamics of Ice Sheets and Glaciers*. Springer Science & Business Media
- 434 Halfar P (1981) On the dynamics of the ice sheets. *J Geophys. Res. Oceans*, **86**(C11), 11065–11072 (doi:  
435 10.1029/JC086iC11p11065)
- 436 Hindmarsh RCA (1996) Stability of ice rises and uncoupled marine ice sheets. *Ann. Glaciol.*, **23**, 105–115 (doi:  
437 10.3189/S0260305500013318)
- 438 Hutter K (1983) *Theoretical Glaciology: Material Science of Ice and the Mechanics of Glaciers and Ice Sheets*,  
439 volume 1 of *Mathematical Approaches to Geophysics*. Springer (doi: 10.1007/978-94-015-1167-4)
- 440 Huybrechts P and Payne T (1996) The EISMINT benchmarks for testing ice-sheet models. *Ann. Glaciol.*, **23**(1),  
441 1–12 (doi: 10.3189/S0260305500013197)
- 442 Jenkins A (2011) Convection-driven melting near the grounding lines of ice shelves and tidewater glaciers. *J. Phys.*  
443 *Oceanogr.*, **41**, 2279–2294 (doi: 10.1175/JPO-D-11-03.1)
- 444 Konrad H, Shepherd A, Gilbert L, Hogg A, McMilan M, Muir A and Slater T (2018) Net retreat of Antarctic glacier  
445 grounding lines. *Nature Geosci.*, **11**, 258–262 (doi: 10.1038/s41561-018-0082-z)
- 446 MacAyeal DR (1989) Large-scale ice flow over a viscous basal sediment: Theory and application to ice stream b,  
447 antarctica. *Journal of Geophysical Research: Solid Earth*, **94**(B4), 4071–4087 (doi: 10.1029/JB094iB04p04071)
- 448 Mitchell I (2004) Demonstrating numerical convergence to the analytic solution of some backwards reachable sets  
449 with sharp features. *Department of Computer Science, University of British Columbia, Vancouver, BC, Canada,*  
450 *Tech. Rep. TR-2004-01*
- 451 Osher S and Fedkiw R (2006) *Level Set Methods and Dynamic Implicit Surfaces*, volume 153 of *Applied Mathematical*  
452 *Sciences*. Springer Science & Business Media (doi: 10.1007/b98879)
- 453 Pattyn F, Schoof C, Perichon L, Hindmarsh RCA, Bueller E, De Fleurian B, Durand G, Gagliardini O, Gladstone R,  
454 Goldberg D and others (2012) Results of the marine ice sheet model intercomparison project, MISMIP. *Cryosphere*,  
455 **6**(3), 573–588 (doi: 10.5194/tc-6-573-2012)

- 456 Picasso M, Rappaz MJ, Reist A, Funk M and Blatter H (2004) Numerical simulation of the motion of a two  
457 dimensional glacier. *Int. J. Numer. Meth. Eng.*, **60**(5), 995–1009 (doi: 10.1002/nme.997)
- 458 Pralong A and Funk M (2004) A level-set method for modeling the evolution of glacier geometry. *J. Glaciol.*, **50**(171),  
459 485–491 (doi: 10.3189/172756504781829774)
- 460 Rignot E, Mouginot J, Scheuchl B, van den Broeke M, van Wessem MJ and Morlighem M (2019) Four decades of  
461 Antarctic Ice Sheet mass balance from 1979-2017. *PNAS*, **116**(4), 1095–1103 (doi: 10.1073/pnas.1812883116)
- 462 Schoof C (2007) Ice sheet grounding line dynamics: Steady states, stability, and hysteresis. *J Geophys. Res. Earth*  
463 *Surf.*, **112**(F3), F03S28
- 464 Schoof C (2010) Ice-sheet acceleration driven by melt supply variability. *Nature*, **468**, 803–806 (doi: 10.1038/na-  
465 ture09618)
- 466 Schoof C and Hewitt I (2013) Ice-sheet dynamics. *Annu. Rev. Fluid Mech.*, **45**, 217–239 (doi: 10.1146/annurev-fluid-  
467 011212-140632)
- 468 Seroussi H, Morlighem M, Larour E, Rignot E and Khazendar A (2014) Hydrostatic grounding line parameterization  
469 in ice sheet models. *Cryosphere*, **8**(6), 2075–2087 (doi: 10.5194/tc-8-2075-2014)
- 470 Sethian JA (1999a) Fast marching methods. *SIAM Rev.*, **41**(2), 199–235 (doi: 10.1137/S0036144598347059)
- 471 Sethian JA (1999b) *Level Set Methods and Fast Marching Methods: Evolving Interfaces in Computational Geometry,*  
472 *Fluid Mechanics, Computer Vision, and Materials Science*. Cambridge University Press, 2nd edition
- 473 Straneo F and Heimbach P (2013) North Atlantic warming and the retreat of Greenland’s outlet glaciers. *Nature*,  
474 **504**, 36–43 (doi: 10.1038/nature12854)
- 475 Van der Veen CJ (1983) A note on the equilibrium profile of a free floating ice shelf. IMAU Report V83-15, Institute  
476 for Marine and Atmospheric Research Utrecht, The Netherlands
- 477 Vieli A and Payne A (2005) Assessing the ability of numerical ice sheet models to simulate grounding line migration.  
478 *J Geophys. Res.*, **110**, F01003 (doi: 10.1029/2004JF000202)
- 479 Vizcaino M, Mikolajewicz U, Ziemen F, Rodehacke C, Greve R and van den Broeke M (2015) Coupled simulations  
480 of Greenland Ice Sheet and climate change up to A.D. 2300. *Geophys. Res. Lett.*, **42**, 3927–3935 (doi:  
481 10.1002/2014GL061142)
- 482 Vogl CJ (2016) A curvature-augmented, REA approach to the level set method. *SIAM J. Sci. Comput.*, **38**(2),  
483 A833–A855 (doi: 10.1137/15M1021258)
- 484 Zhao HK, Chan T, Merriman B and Osher S (1996) A variational level set approach to multiphase motion. *J. Comput.*  
485 *Phys.*, **127**(1), 179–195 (doi: 10.1006/jcph.1996.0167)